coatings

MDPI

Article

Thin Films Characterization and Study of N749-Black Dye for Photovoltaic Applications

Muhammad Tahir [1,*], Ikram Ud Din [1], Muhammad Zeb [1], Fakhra Aziz [2], Fazal Wahab [3], Zahid Gul [1], Alamgeer [1], Mahidur R. Sarker [4,*], Sajad Ali [1], Sawal Hamid Md Ali [5,*] and Ioannis Kymissis [6]

1 Department of Physics, Faculty of Physical and Numerical Sciences, Abdul Wali Khan University Mardan, Mardan 23200, Pakistan
2 Department of Electronics, Jinnah College for Women, University of Peshawar, Peshawar 25120, Pakistan
3 Department of Physics, Karakoram International University, Gilgit 15100, Pakistan
4 Institute of IR 4.0, University Kebangsaan Malaysia, Bangi 43600, Malaysia
5 Department of Electrical, Electronic and Systems Engineering, Faculty of Engineering and Built Environment, University Kebangsaan Malaysia, Bangi 43600, Malaysia
6 Department of Electrical Engineering, Columbia University, New York, NY 10027, USA
* Correspondence: tahir@awkum.edu.pk (M.T.); mahidursarker@ukm.edu.my (M.R.S.); sawal@ukm.edu.my (S.H.M.A.)

Abstract: This paper reports on the fabrication and photovoltaic characteristics of a heterojunction solar cell based on an organic small molecular semiconductor, N-749 black dye (N749-BD). To investigate the photovoltaic characteristics of N749-BD, an ITO/PEDOT:PSS/N749-BD/Ag device is prepared by spin casting a 100 ± 5-nm thin film of N749-BD on the poly(3,4, ethylene dioxythiophene):polystyrene sulfonate (PEDOT:PSS) film, which acts as buffer/hole transport layer (HTL) and indium tin oxide (ITO) is employed as a transparent conducting substrate. Under standard testing conditions (STC), i.e., 25 °C, 1.5 AM global and 100 mW/cm^2 irradiation, the photovoltaic parameters of the device, such as fill factor (FF) and power conversion efficiency (PCE), are found to be 0.65 and 3.8% ± 0.5%, respectively. Current-voltage (*I–V*) characteristics of the device are also studied in dark conditions to measure reverse saturation current (I_0), series resistance at the interface, rectification ratio (RR), barrier height (ϕ_b) and ideality factor (n). Optical bandgaps (E_g) of N749-BD thin film are found by applying Tauc's plot on its ultraviolet-visible (UV-Vis) spectrum, which are measured to be 1.68, 2.67, 3.52 and 4.16 eV. External quantum efficiency (EQE) measurements of the fabricated device are studied, which demonstrate large value of EQE ≈ 12.89%, with peak intensity at 626 nm. Bond dynamics and compositional analysis of N749-BD is carried out via Fourier transformed infrared (FTIR) spectroscopy. Morphology of the thin film of N749-BD on quartz glass are investigated via scanning electron microscopy (SEM) with in-situ energy dispersive X-ray (EDX) spectroscopy which exhibits random distribution of N749-BD grains across the surface with nearly uniform grain sizes and shapes. The larger values of FF, PCE and EQE of ITO/PEDOT:PSS/N749-BD/Ag device suggests the potential of N749-BD to be utilized in low cost, simple manufacturing process and high performance of solar cells.

Keywords: phtovoltaic properties; N749 black dye (BD); organic solar cell; external quantum efficiency (EQE); current-voltage (*I–V*) properties

Citation: Tahir, M.; Din, I.U.; Zeb, M.; Aziz, F.; Wahab, F.; Gul, Z.; Alamgeer; Sarker, M.R.; Ali, S.; Ali, S.H.M.; et al. Thin Films Characterization and Study of N749-Black Dye for Photovoltaic Applications. *Coatings* **2022**, *12*, 1163. https://doi.org/10.3390/coatings12081163

Academic Editor: Ni Yang

Received: 28 April 2022
Accepted: 3 July 2022
Published: 12 August 2022

1. Introduction

Harvesting the full solar spectrum is a massive challenge to fulfill energy demand in the present era; thus, researchers and engineers are constantly exploring novel functional materials and methods for photovoltaic applications. These efforts are aimed to enhance the overall power conversion efficiency (PCE), lifetime and/or stability and to lower the production cost of solar cells. Recently, newly developed techniques and architectures for device fabrication, including organic bulk heterojunction (BHJ) solar cells (SCs) [1],

dye-sensitized solar cells (DSSCs) [2,3] perovskite solar cells (PSCs) [4] and tandem SCs have paved the way towards next-generation solar cells [5]. SCs are made with various designs, such as nanostructures, layer-by-layer architectures, heterojunctions, and so on, to achieve higher conversion efficiencies. Many of the devices can have heterojunction interfaces. Lasers, diodes, sensors, SCs and transistors are some examples of heterojunction created between inorganic and/or organic semiconductors [6]. The organic heterojunction structures have become a standard platform for small molecular and polymeric photovoltaic (PV) application [7]. The architectures of these heterojunctions have a significant impact on the devices' efficiency, durability and electrical characteristics [8–10].

Dyes are compounds that are used to give materials like textiles, paper, and leather a solid color. However, they have been widely used as sunlight harvesters in the DSSC for sensitization to attain higher efficiencies. Dyes are categorized in two basic areas; one is the metal-based organic dyes, which include ruthenium complexes, e.g., N3 dye, N719 dye and N749-BD, while the second category is metal-free organic dyes that use donor and acceptor materials in a junction [11]. The metal based ruthenium complexes are some of the benchmark sensitizers for DSSCs, which achieve above 10% efficiency due to their broad optical absorption spectrum and higher current density (J_{sc}) values [12]. The ruthenium dye N749-BD is a panchromatic dye that belongs to the ruthenium family. N749-BD is one of the best dye sensitizers because of its interesting electronic and optoelectronic properties with the advantages of excellent absorption of light over a broad range in the visible spectrum and thermal and chemical stabilities at ambient conditions [13,14]. Being an organic dye, N749-BD has the advantages of mechanical flexibity, low cost, facile processability for thin film growth and device fabrication over the inorganic semiconductors, such as CdS, Si and SnS [15]. Despite its dark green hue, it has gained the name "black dye" in the dye-sensitized SCs community due to its significant absorption in a wide range of visible light (~920 nm). In DSSCs, dye molecules play a vital role in light-harvesting efficiency, which establishes a PCE threshold. Numerous molecular sensitizers have been exploited in DSSCs, which include N719, N3 and N749 [16–18]. Notably, only N749-BD has the potential to extend the light absorption spectrum to the red and near-infrared (NIR) range, which makes it capable of achieving higher light harvesting efficiency and, hence, higher PCE of a device [19]. N749-BD has been extensively explored in the dye-sensitized solar cells (DSSCs) [20–22]; however, it is hardly ever used in thin film-based PV devices. Due to the aforementioned advantages of N749-BD, it has been employed for the first time in thin film layer-by-layer structure-based SCs with PEDOT:PSS as a hole transport layer (HTL) as well as a buffer layer to study its potential use for PCE. Although N-749 BD possesses extraordinary properties which are necessary for an active solar cell material, the thin film deposition of N-749 BD is a tricky part in the fabrication of ITO/PEDOT:PSS/N749-BD/Ag solar cell, since, N-749 BD is difficult to evaporate via vacuum thermal deposition as well as difficult to make its solution in organic solvents. To make a uniform solution of N-749 BD, it is continously stirred in ethanol at the relatively elevated temperature at 60 °C for approximately 72 h.

Herein, we aim to fabricate N749-BD-based layer-by-layer ITO/PEDOT:PSS/N749-BD/Ag heterojunction SCs by a facile spin coating technique for its potential in photovoltaic applications. In the device, PEDOT:PSS serves as a buffer layer and HTL to facilitate hole transport across the device. The aim of this work is to realize the potential of N749-BD as an active material in SCs for energy harvesting applications. N749-BD thin films' structural, morphological and optical features are also investigated and connected with device performance. In the present study, from the performace of N-749 BD in layer-by-layer structred solar cell, it can be suggested that N-749 BD may be one of the best materials for high-performance DSSCs used in combination with different HTL and electron transport layer (ETL) materials. Therefore, the device design and architecture could be extended to fabricate multi-layer solar cells for better performance. This facile spin coating and low-temperature fabrication of N-749 BD based devices could reduce the manufacturing cost and increase the productivity of solar cells.

2. Materials and Methods

2.1. Material and Device Preparation

PEDOT: PSS (pH value 1.5, molar ratio 1.00:5.26 and viscosity 8 mPa.s) and N749-BD are obtained from Sigma Aldrich (Petaling Jaya, Malaysia) and used as received. Figure 1a,b shows the molecular structures of PEDOT: PSS and N749-BD, correspondingly. The pre-patterned ITO coated on glass and quartz glasses are used as substrates for heterojunction device and morphological study of N749-BD thin films, respectively. The substrates are first cleaned in acetone followed by isopropanol using ultrasonic bath for 15 min in each solvent and, afterwards, are dried with dry nitrogen (N_2) gas. A 20-nm layer of PEDOT:PSS (from solution of 10 wt.% in water) is deposited on the cleaned ITO substrate by using spin coater (Holmarc Model no: HO-TH-05, Global Analytical Co., Ankara, Turkey) at 2000 rpm for 20 s. Later, the samples are kept on hotplate for 2 h at 50 °C under N_2 gas flow in order to evaporate solvent. A uniform solution of N749-BD is prepared in ethanol at a concentration of 20 mg/mL using a magnetic stirrer. The solution of N749-BD is then spin-coated at the rate of 2000 rpm for 30 s on PEDOT:PSS/ITO. The sample is dried using a hotplate as mentioned previously. Lastly, an 80-nm-thick layer of silver (Ag) electrode is thermally evaporated on top of the N749-BD layer using an Edwards Auto-306 vacuum thermal evaporator to complete the formation of the ITO/PEDOT:PSS/N749-BD/Ag device. The chamber pressure is maintained at 1.5×10^{-5} mbar during thermal deposition, with a deposition rate of roughly 0.2 nm/s. Figure 1c,d shows the schematic figure and energy level diagram of the fabricated ITO/PEDOT:PSS/N749-BD/Ag device, respectively.

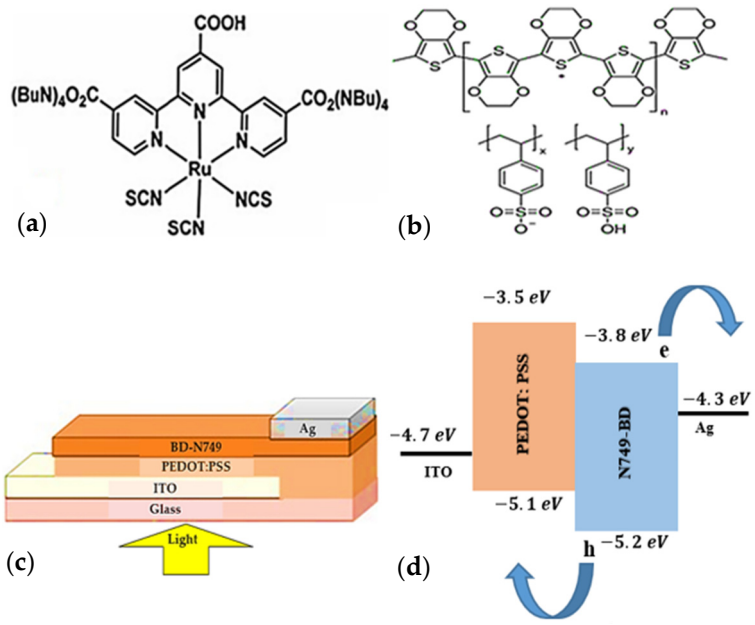

Figure 1. Molecular structure of (**a**) N749-BD and (**b**) PEDOT:PSS; (**c**) architecture of fabricated ITO/PEDOT:PSS/N749-BD/Ag solar cell; and (**d**) energy level diagram of the materials used in the device.

2.2. Device and Thin Films Characterization

UV-Vis and FTIR spectroscopic studies are performed to determine bandgap and structural information and/or bond dynamics of N749-BD, respectively. A PerkinElmer Lambda 1050 UV/vis/NIR spectrometer is used to measure the UV-Vis spectrum, and PerkinElmer Spectrum™ 3 FT-IR spectrometer is used for FTIR spectrum. Morphology and elemental analysis of N749-BD films are studied by scanning electron microscopy (SEM) (JEOL JSM-591, Tokyo, Japan) with in situ energy dispersive X-ray (EDX) spectroscope. For crystallinity and phase analysis of N749-BD, an X-ray diffraction (XRD) instrument (JEOL, JDX-3532, Tokyo, Japan) is used. For photovoltaic measurements of ITO/PEDOT:PSS/N749-

BD/Ag device, a Newport Oriel solar simulator with 1.5 AM filters, 25 °C and 100 mW/cm^2 is used. The *I–V* characteristics in dark condition are measured using an SMU Keithley-236.

3. Results

3.1. N749-BD Thin Films Characteristics

SEM images of thin film of N749-BD are shown in Figure 2a and inset of Figure 2a with low and high resolutions, respectively. These images reveal slightly non-uniform surface features with granular structure of N749-BD that are nearly uniformly distributed throughout the surface of the film. However, at a few places, there is some non-uniformity and agglomeration of grains, which might be due to the uneven and high growth rate deposition of N749-BD film during the spin-coating process. Charge carriers localize due to charge trapping and interfacial states as a result of the irregularity and roughness of the film. For the purpose of elemental analysis, the EDX spectrum of N749-BD is shown in Figure 2b that exhibits various peaks at different energy (keV) on the x-axis. Each peak specifies the presence of different corresponding elements in N749-BD film. EDX analysis shows that N749-BD film is composed of carbon, oxygen, sulfur, nitrogen and ruthenium, with different proportions/percentages, which are shown in Table 1.

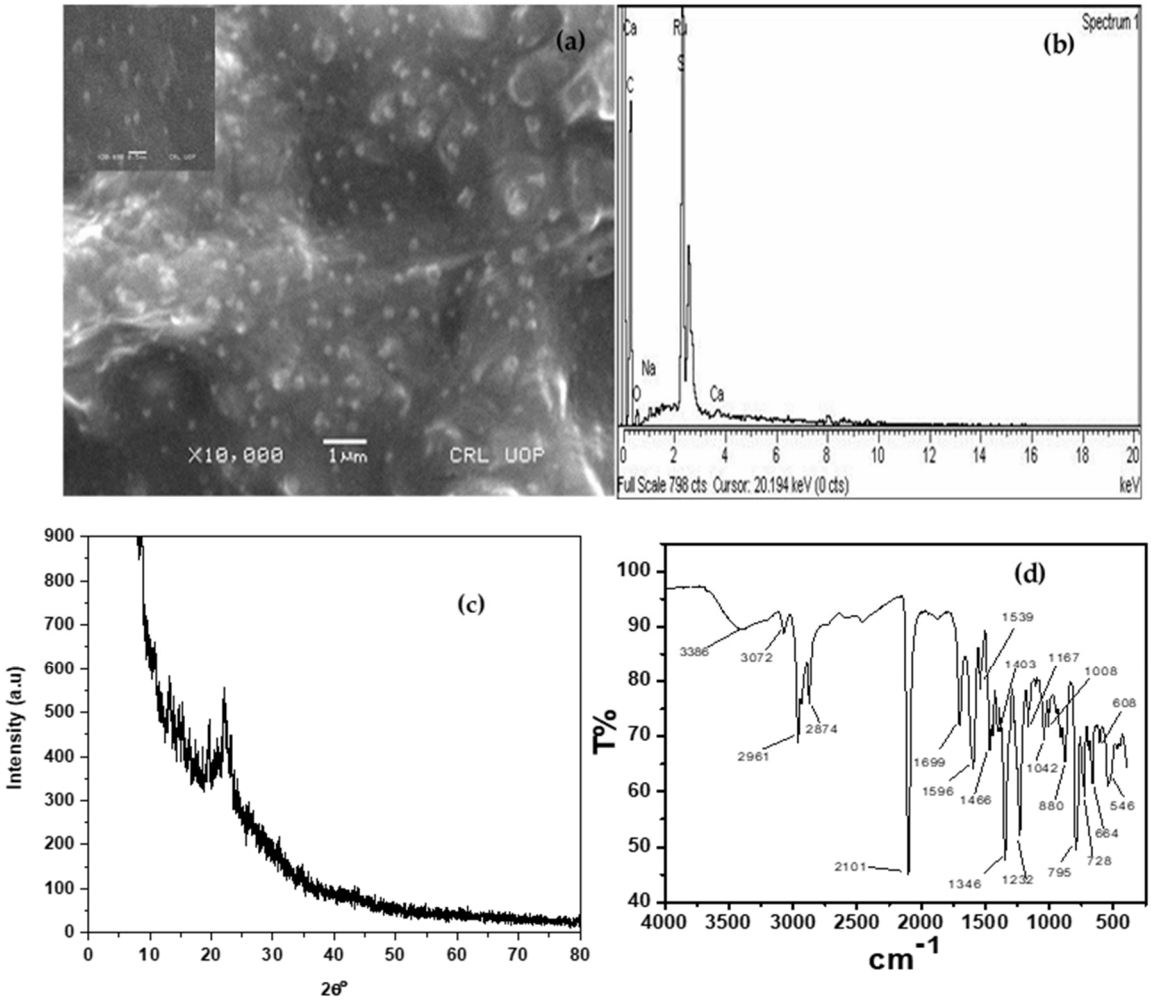

Figure 2. (**a**) SEM micrographs; (**b**) EDX spectrum; (**c**) XRD pattern and (**d**) FTIR transmission spectrum of N749-BD thin film.

Table 1. Elemental analysis of N749-BD film.

Element	Weight (%)	Atomic (%)
C K	70.66	89.26
O K	2.26	2.14
Na K	0.44	0.29
S K	13.08	6.19
Ca K	0.38	0.14
Ru L	13.18	1.98

The XRD method is utilized to study the crystal nature, i.e., crystalline, polycrystalline or amorphous, of N749-BD [23]. The XRD spectrum of the N749-BD film deposited on pre-cleaned quartz glass is obtained at room temperature, which is shown in Figure 2c. The absence of any significant peak in the spectrum demonstrates the amorphous nature of N749-BD. Furthermore, the flat-curve obtained from the diffractogram also reveals the amorphous nature of the semiconductor [24]. A small peak at around 22° indicates a slight degree of crystallinity of the N749-BD. However, the overall nature of N749-BD is amorphous, which can also be linked with the SEM phase study.

Bond dynamics and chemical structure/functional group analysis of N749-BD film is studied from the FTIR spectrum as shown in Figure 2d. The N749-BD film is probed with infrared radiation, and transitions between vibrational energy levels are measured as transmission spectrum at different energies (cm^{-1}) as shown in Figure 2d. The peaks occurring at 3072 and 2961 cm^{-1} identify a single bond between carbon and hydrogen (C–H), and the mode of vibration is stretching. The carbon-nitrogen double bond (C=N) is identified by the peaks at 1699 and 1596 cm^{-1}, while the carbon-nitrogen single bond (C–N) is verified by the peaks at 1167 and 1042 cm^{-1}. The peaks appearing at 1466 and 1403 cm^{-1} confirm the presence of carbon-carbon single bond (C–C). The carbon oxygen single bond (C–O) stretch occurs at 1232 cm^{-1}. In the figure, the most intense absorption peak at 2101 cm^{-1} verifies the presence of thiocyanate ligands (–N=C=S). All the labeled peaks in Figure 2d justify the chemical structure, composition and bonds of N749-BD. Table 2 presents all the peaks at different energies and their corresponding bond dynamics.

Table 2. Bond dynamics in N749-BD film.

Peaks at Energy (cm^{-1})	Bonds Nature/Dynamics
728	Out-of-Plane C–H Bend
795	In-Plane C–H Bend
880	Out-of-Plane C–H Bend
1042	In-Plane C–H Bend
1232	In-Plane C–H Bend
1346	In-Plane Pyrrole Stretch
1466	C–C Benzene Stretch
1596	C–C Benzene Stretch
1699	C–C Benzene Stretch
2101	C–H Stretch

Optical absorption width and bandgap of N749-BD is found from the UV-Vis spectrum as shown in Figure 3a. The spectrum reveals that N749-BD demonstrates better light absorption and/or harvesting efficiency with broad spectral range from UV to NIR, i.e., 290–800 nm. Such broad and large optical absorption make N749-BD one of the best candidates for harvesting the large number of incident photons that contributes to higher PCE of solar cells [20,21]. Also, it can be seen from the diagram shown in Figure 1d that materials used in the device have higher bandgaps, which contribute to the larger values of V_{oc} and smaller values of I_{sc} of the device. The value of V_{oc} increases with bandgap because the recombination current falls. However, at very large bandgaps, there is dramatic decrease in V_{oc} because of very low I_{sc}. The value of V_{oc} is also limited by the charge

recombination. The relationship between the V_{oc} and bandgap (E_g) can be understood from the following equations [25–27]:

$$J_0 = qn_i^2\left[\frac{D_N}{L_N N_A} + \frac{D_P}{L_P N_D}\right] \quad (1)$$

$$n_i^2 = N_c N_v e^{[(E_v - E_c)/kT]} = N_c N_v e^{(-E_g/kT)} \quad (2)$$

$$V_{oc} = \frac{kT}{q}\ln\left(\frac{J_{ph}}{J_0} + 1\right) \quad (3)$$

where, in Equation (1), J_0 is the reverse saturation current density, q is the electronic charge, n_i is the intrinsic carriers' density, $D_N = V_T \cdot \mu_N$ is the electron diffusion constant with V_T as thermal voltage and μ_N as electron mobility, L_N is the electron diffusion length, N_A is the acceptor concentration, $D_P = V_T \cdot \mu_P$ is the hole diffusion constant with V_T as thermal voltage and μ_P as hole mobility, L_P is the hole diffusion length and N_D is the donor concentration. In Equation (2), N_c is the effective density of states in conduction band, N_v is the effective density of states in valence band, E_v is the valence band energy, E_c is the conduction band energy, E_g is the bandgap energy, k is the Boltzmann constant and T is the absolute temperature. Equation (3) presents V_{oc} as open circuit voltage and J_{ph} is photo-generated current density. From Equation (2), it can be seen that n_i decreases with increase in E_g, and from Equation (1), it can be observed that J_0 is decreased with the decrease in n_i, whereas, from Equation (3), V_{oc} is increased as J_0 decreases; hence, consequently, V_{oc} increases with increase in E_g and vice versa [28].

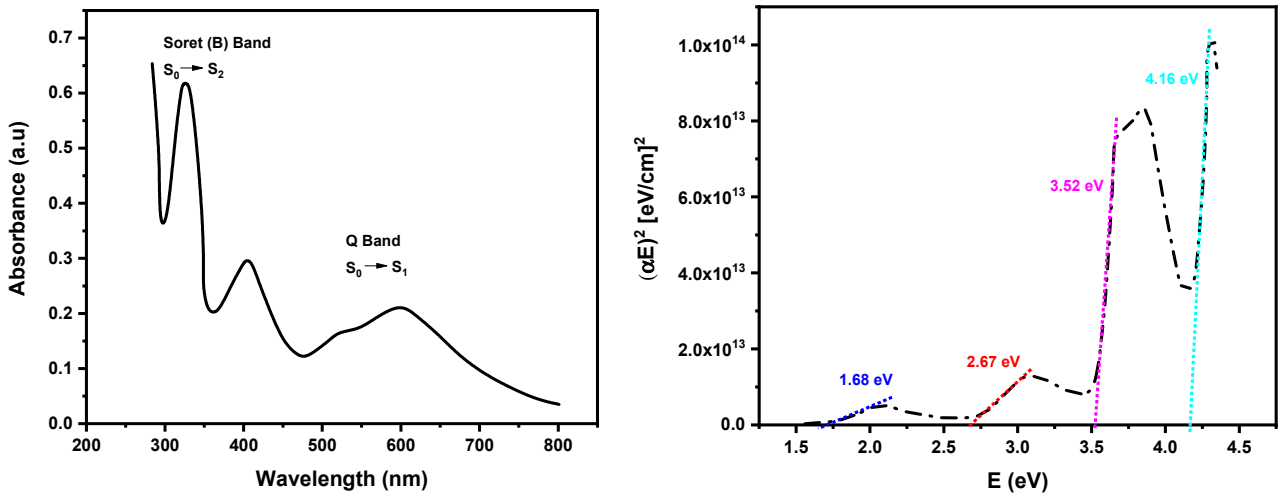

Figure 3. (**a**) UV-Vis absorption spectrum and (**b**) optical energy bandgap of N749-BD.

Due to highly conjugated π-electrons in N749-BD, its electronic spectrum is comprised of two different bands, the Soret or B-band and Q-band. The former band occurs at relatively higher energy with intense peaks in the UV region, while the later happens in the visible region with comparatively weak peaks. Figure 3a exhibits three prominent peaks in the Soret or B band at 290, 330 and 406 nm, which are ascribed to the intra-ligand π–π^* transitions from ground states (S_0) to the second or higher excited states (S_2 or S_n). Another peak is evident in the Q-band at ~600 nm that can be attributed the transition from ground state to the first excited state (S_0–S_1) and also to metal-to-ligand charge transfer complexes. The results shown in Figure 3a are in good agreement with those reported elsewhere [29,30].

To calculate optical bandgap of N749-BD, the following Tauc's relation [31] is used:

$$\alpha E = (E - E_g)^{\theta} \quad (4)$$

where E_g represents energy bandgap, E is incident photon energy, θ is the transition constant and α is absorption coefficient that can be found as:

$$A = -\ln\left(\frac{I}{I_0}\right) \quad (5)$$

$$\Rightarrow A = \alpha d \quad (6)$$

Here, A is absorbance, and d is the thickness of N749-BD film. The transition constant θ equals to 2 for indirect transition and $\frac{1}{2}$ for direct transition between the energy levels. Since N749-BD is a direct bandgap semiconductor, the direct transition model is adopted to calculate the value E_g of N749-BD. According to Equation (1), (αE^2) is plotted versus E, as shown in Figure 3b, and the intercept of the slope of linear regions in the curve at zero y-axis gives the value of E_g. The E_g values for N749-BD are found to be 1.68 eV, 2.67 eV, 3.52 eV and 4.16 eV. The later higher values of bandgaps correspond to the UV region, whereas the former smaller values are due to the visible spectrum. In the visible range, the values of E_g are in good agreement with those reported in the literature [29,32].

3.2. Current-Voltage (I–V) Characteristics

3.2.1. I–V Characteristics in Dark

The *I–V* measurements of ITO/PEDOT:PSS/N749-BD/Ag device in dark conditions at 25 °C are investigated to find and understand the heterojunction/interfacial properties. Figure 4a shows an asymmetrical *I–V* curve that demonstrates a rectifying and non-ohmic nature of the ITO/PEDOT:PSS/N749-BD/Ag device. Current rectification ratio (RR) and turn-on voltage V_{TO} are found to be 57.2 at ±2.3 V and 1.86 V, respectively. In the forward voltage region, the interfacial states, series resistance (R_s) and depletion region/barrier height ϕ_b formed between N749-BD layer and ITO strongly affect the exponential behavior of the *I–V* characteristics. The quality of the interface/heterojunction is characterized by the ideality factor (n) that provides sufficient information and understanding about the device performance. In reverse bias, reverse saturation current determines the amount of minority charge carriers across the heterojunction [33,34]. The values of R_s and shunt resistance (R_{sh}) are ~31 kΩ and 0.13 GΩ, respectively, which are found from the voltage (V) vs. dV/dI (R_j) relation as shown in Figure 4c. Usually, when the value of R_s is very small compared to R_{sh} i.e., $R_s \ll R_{sh}$, the performance of solar cells is better. The R_s is an undesired and parasitic parameter that in fact limits current through the heterojunction and, hence, results in lower value of RR of the device in dark conditions. This parasitic effect of R_s further adversely affects the value of n, which influences the quality of the ITO/PEDOT:PSS/N749-BD/Ag device. Different layers in the ITO/PEDOT:PSS/N749-BD/Ag solar cell, such as internal interface layers between PEDOT:PSS/N749-BD, lateral conduction through the transparent conducting oxide ITO and Ag contact set up *Rs*. In ideal heterojunction devices, the values of *Rs* and n are zero (0) and one (1), respectively. However, for actual devices, the values of *Rs* and n deviate from ideal behavior (i.e., $Rs > 0$ and $n > 1$) due to interface states and potential barriers. In solar cells, the main role of series resistance is to decrease the value of fill factor (FF), although extremely higher values of R_s may also lessen the short-circuit current (I_{sc}). Due to these undesirable effects of R_s, it is known as a parasitic parameter. However, in the present study, the obtained value of R_s ~31 kΩ is still lower than that of other small molecular semiconductors reported elsewhere [35]. By using Equations (7)–(10) [34], the other key junction parameters of the device such as n, ϕ_b and I_0 are calculated from the log-linear scale (ln(I)-V) of *I–V* characteristics as shown in the inset of Figure 4a, which are 7.7, 0.98 eV and 1.6×10^{-7} A, respectively.

$$I = I_0\left[\exp\left(\frac{q(V - IR_s)}{nkT}\right) - 1\right] \quad (7)$$

where q is electronic charge, k is Boltzmann constant, R_s is the series resistance that should be smaller than the shunt resistance ($R_s \ll R_{sh}$) and T is absolute temperature.

$$I_0 = AA^*T^2 \exp\left(\frac{-q\phi_b}{kT}\right) \tag{8}$$

where 'A' is the active area of device, A^* is Richardson constant ($A^* = 1.3 \times 10^5$ A cm^{-2} K^{-2} for ITO substrate) [36].

$$n = \frac{q}{kT}\frac{dV}{d(\ln I)} \tag{9}$$

$$\phi_b = \frac{kT}{q}\ln\left(\frac{AA^*T^2}{I_0}\right) \tag{10}$$

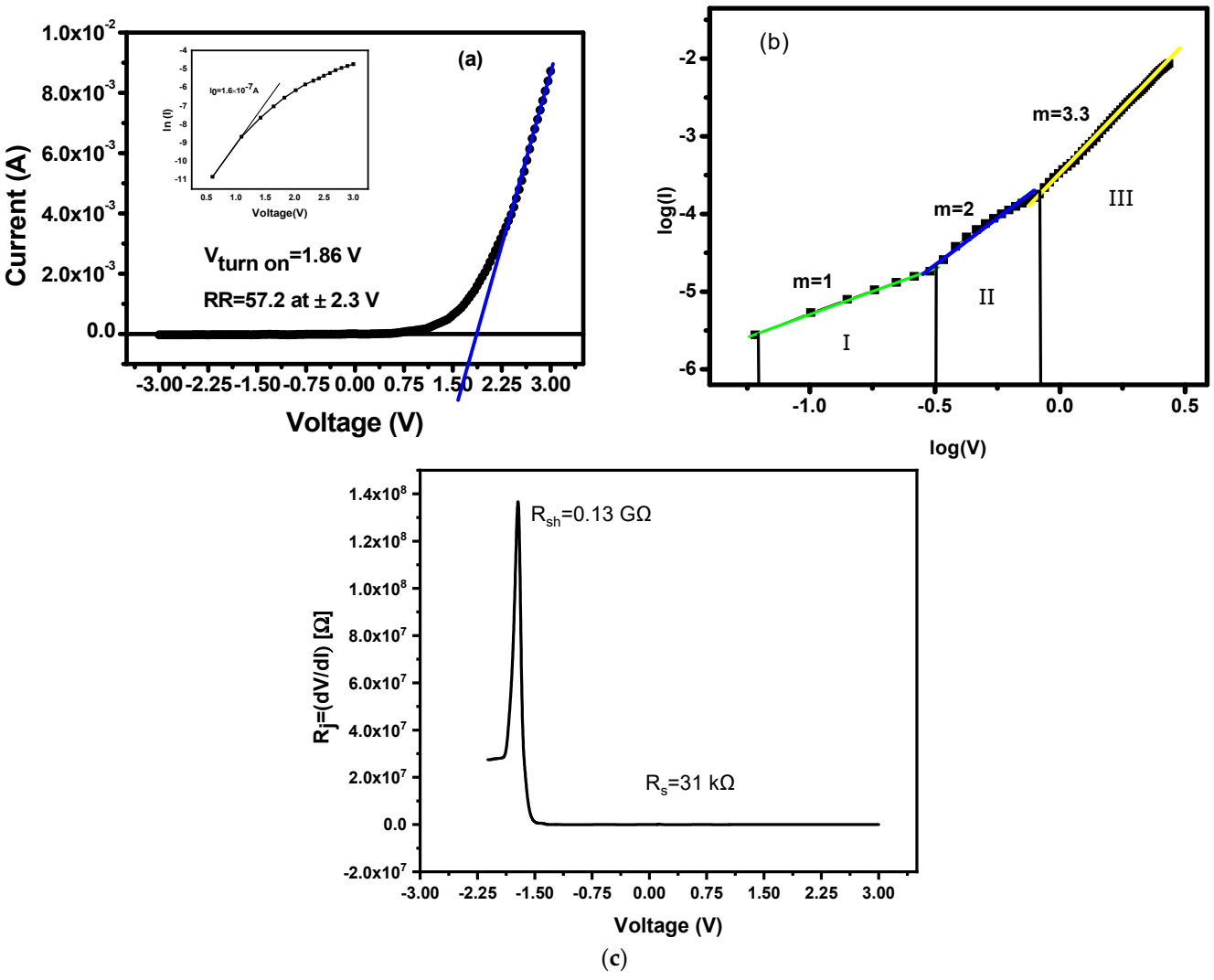

Figure 4. (**a**) *I*–*V* graph (in dark), (**inset**) semi-log I-V graph; (**b**) log *I*-log *V* curve; and (**c**) series and shunt resistance graph of ITO/PEDOT:PSS/N749-BD/Ag heterojunction.

The charge conduction mechanism in the ITO/PEDOT:PSS/N749-BD/Ag heterojunction can be explained from the log *I*-log *V* graph, as shown in Figure 4b, by applying Power law/Child's law, i.e., $I \approx V^m$ [37], whereas m is a slope of a linear region of the curve shown in Figure 4b, and different values of m indicate different conduction processes. When $m = 1$, i.e., $I \approx V$, it indicates an ohmic conduction process, and, hence, there is no rectification in current by applying voltage. When $m = 2$, the relation becomes $I \approx V^2$,

which shows the space-charge-limiting current (SCLC) region that is associated with the depletion region and is responsible for asymmetrical *I–V* characteristics as well as for current rectification across the heterojunction. When the value of $m > 2$, it demonstrates the trapped-charge-limiting current (TCLC) region [38], which is attributed to various traps, i.e., shallow and/or deep traps, at the heterojunction that are responsible for limiting the current flow across the device. For the ITO/PEDOT:PSS/N749-BD/Ag device, there can be seen three distinct regions, I, II and III, in the logI-logV graph shown in Figure 4b, which describe ohmic conduction at beginning at $m = 1$, SCLC conduction mechanism at $m = 2$ and TCLC process at $m = 3.3$, respectively. Since the ITO/PEDOT:PSS/N749-BD/Ag device shows an asymmetric *I–V* curve and rectifying behavior, as shown in Figure 4a, its dominant conduction is an SCLC mechanism. In SCLC, the density of charge-carriers injected is much higher than that of thermally generated free charge-carriers which leads to current rectification.

3.2.2. Photovoltaic I–V Characteristics

For the evaluation of an organic solar cell performance and enhancement in architecture and fabrication, the deep insight of electrical parameters from current-voltage characteristic is indispensable. Many losses can be observed in the organic solar cells that affect the power conversion efficiency (PCE); these losses are linked to parameters, such as I_{sc}, FF and open circuit voltage (V_{oc}). Also, the main device parameters, i.e., n, R_s, R_{sh} and I_0 are the factors that can manage the losses. The R_{sh} in solar cells usually originates from the defects that are developed during the fabrication process, which provide an alternate conducting path for the photo-generated charge carriers. The decrease in the value of R_{sh} can adversely affect the PCE of solar cells by reducing the values of V_{oc} and FF.

The photovoltaic measurements of the ITO/PEDOT:PSS/N749-BD/Ag device are presented as current density (J) vs. V graph as shown in Figure 5, which is measured at STC, i.e., 100 mW/cm^2, AM 1.5 G and 25 °C. The graph shows that photocurrent through the gadget is larger in the light than in the dark. The higher value of J is ascribed to creation of the excitons (electron-hole pairs) in the absorber layer (N749-BD film), which dissociate into separate electrons and holes at the interface of the heterojunction, leading to excess of photocurrent. To measure photovoltaic performance of the ITO/PEDOT:PSS/N749-BD/Ag device, quantitative values of fill factor (FF) and PCE are calculated using the following relations:

$$\mathrm{FF} = \frac{V_{\max} J_{\max}}{V_{oc} J_{sc}} \tag{11}$$

and

$$\mathrm{PCE}(\eta) = \mathrm{FF}\frac{J_{sc} V_{oc}}{EA} \times 100 \tag{12}$$

where $V_{\max}$, $J_{\max}$, V_{oc} and J_{sc} are maximum voltage, maximum current density, open circuit voltage and short circuit current, respectively, whereas in Equation (12), E represents the solar irradiance, and A is the active area of device.

The values of V_{oc}, J_{sc} and FF are measured as 0.88 V, 6.0 mA/cm^2 and 0.65, respectively. From Equation (12), PCE for the ITO/PEDOT:PSS/N749-BD/Ag device is calculated to be 3.8% ± 0.5%.

The higher value of FF can be ascribed to the enhanced values of $V_{\max}$ and $J_{\max}$ which might be due to strong and wide spectral absorption of light in the bulk of the N749-BD layer. Thus, more excitons are generated, which get dissociated at the interface of N749-BD/ITO. Moreover, the improved J_{sc} of the device can be attributed to (1) lower charge recombination in N749-BD layer and (2) large interface surface area that gives rise to enhanced charge carrier transport [39,40].

Another important parameter that quantitatively describes performance of solar cells is the external quantum efficiency (EQE), which is the ratio of number of electron-hole pairs

collected at the electrodes to number of incident photons absorbed at zero voltage (0 V). Mathematically, EQE is expressed as follows:

$$\mathrm{EQE}(\lambda) = \frac{I_{sc}(\lambda)hc}{q\lambda P_A} \tag{13}$$

where the parameters λ, I_{sc}(λ), h, c, q, P_A(λ) are wavelength of the incident light, short-circuit current, Planck's constant, speed of light, electronic charge and the power of incident light, respectively.

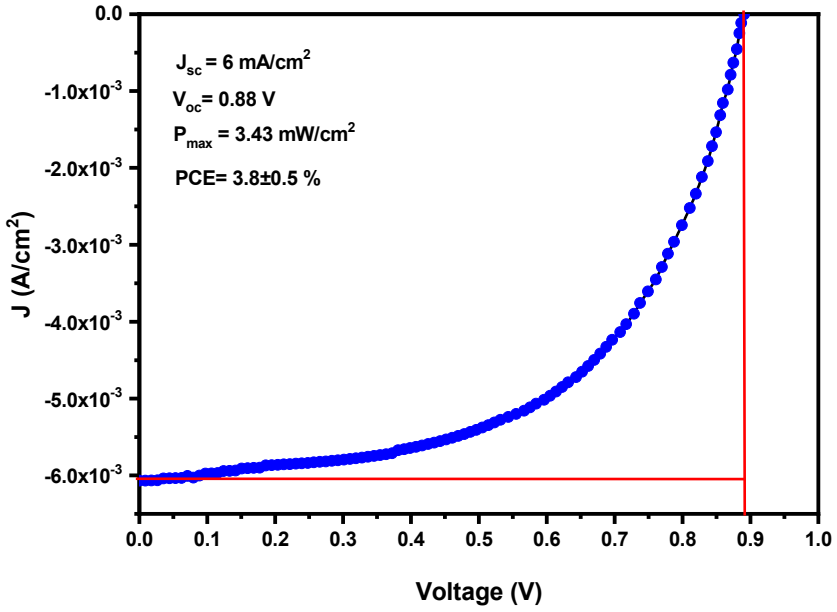

Figure 5. J-V graph of ITO/PEDOT:PSS/N749-BD/Ag device.

The EQE spectrum of the ITO/PEDOT:PSS/N749-BD/Ag device is shown in Figure 6a. There are two peaks in Figure 6, one at 532 nm and the other at 626 nm, which can be attributed to N749-BD absorptions. At the relatively higher peak 626 nm, EQE value is about 12.89%. In addition to the material (N749-BD) properties, EQE is strongly affected by light absorption, exciton diffusion, exciton dissociation and charge carrier transport. Also, the spectrum of incident power is shown in Figure 6b.

Compared with earlier reported organic solar cells, the device based on N749-BD showed relatively larger V_{oc} and FF, which remarkably influenced the performance of ITO/PEDOT:PSS/N749-BD /Ag solar cells. Table 3 presents a comparison of the present work with the previously reported work done on small organic molecular semiconductors and dyes.

Table 3. Comparison of parameters of ITO/PEDOT:PSS/N749-BD/Ag solar cells with previously reported solar cells.

Heterojunction Structure	*FF* (%)	V_{oc} (V)	J_{sc} (mA/cm^2)	*PCE* (%)	References
Al/BCP/C_{60}/PtOEP/PEDOT/ITO	42	0.58	5.0	1.2	[41]
Ag/ZnPc/PEDOT:PSS/ITO	48	0.55	5.01	2.8	[39]
N719	39	0.65	3.33	0.86	[42]
Z907	38	0.71	3.70	1.01	[43]
N3	47	0.53	11	2.78	[43]
ITO/PEDOT:PSS/N749-BD/Ag	65	0.88	6.0	3.8 ± 0.5	Present work

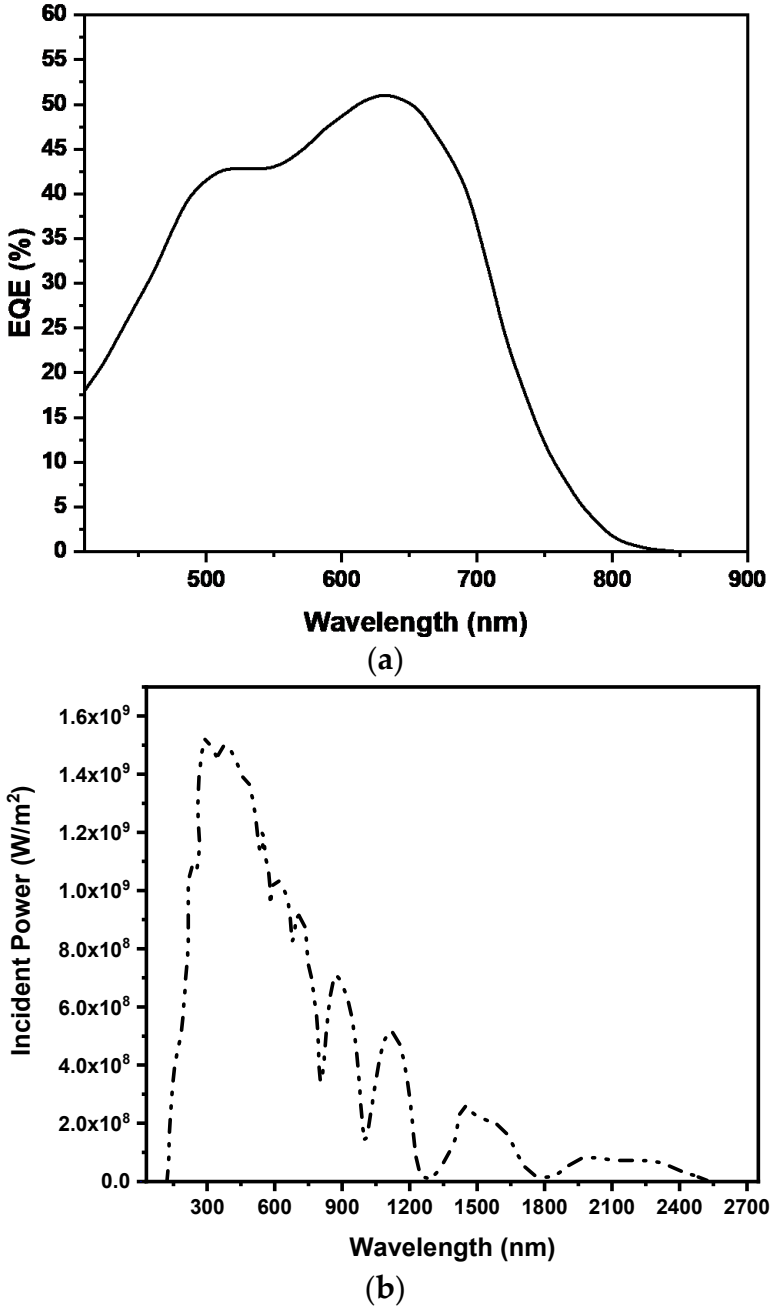

Figure 6. (**a**) EQE spectrum of ITO/PEDOT:PSS/N749-BD/Ag solar cell; (**b**) spectrum of incident light.

4. Conclusions

In this work, an ITO/PEDOT:PSS/N749-BD/Ag heterojunction device is fabricated using N749-BD as an active layer for its potential in photovoltaic applications. The fabricated device is first studied under dark conditions to explore its various heterojunction parameters, such as n, R_s, ϕ_b and I_0, which exhibited better performance and quality of device interfacial properties. At STC, the photovoltaic measurements of the device revealed larger values of FF and PCE, which are calculated to be 0.65 and 3.8% $\pm$ 0.5%, respectively. The higher value of PCE is evident from the strong and broad UV-vis absorption and larger value of EQE $\approx$ 12.89%, with peak intensity at 626 nm. The most probable values of optical bandgap E_g of N749-BD are 1.8 and 2.69 eV, which are measured using Tauc's equations. SEM images showed nearly uniform grain distribution at the film surface of N749-BD. XRD and FTIR confirm amorphous nature and the corresponding chemical com-

position/bond dynamics of N749-BD, respectively. These remarkable properties—strong and broad absorption of the UV-vis and higher FF, EQE and PCE—suggest N749-BD to be one of the promising candidates for SC applications, equally beneficial in tandem and DSSC structures.

Author Contributions: Conceptualization, M.T. and I.U.D.; methodology, M.T., A., F.W. and F.A.; software, M.T., A. and S.A., I.U.D.; validation, F.A., A., M.R.S. and M.T.; formal analysis, M.T. and M.R.S.; investigation, M.T., Z.G. and M.Z.; resources, M.T., F.W. and M.Z.; data curation, M.T., S.A. and M.R.S.; writing—M.T., F.W. and I.U.D.; writing—review and editing, M.T., I.K., F.A., Z.G., S.H.M.A. and M.R.S.; supervision, M.T.; project administration, M.T.; funding acquisition, S.H.M.A. All authors have read and agreed to the published version of the manuscript.

Funding: Universiti Kebangsaan Malaysia (UKM) for funding the research under Grant Code GGPM-2021-050.

Institutional Review Board Statement: Not applicable.

Informed Consent Statement: Not applicable.

Data Availability Statement: Not applicable.

Acknowledgments: All the authors are grateful to the Abdul Wali Khan University Mardan, Pakistan, Higher Education Commission (HEC) of Pakistan, for providing the research facilities and Project. No. 10170/KPK/NRPU/R&D/HEC/2017 and Project No. 7180/GilgitBaltistan/NRPU/R&D/HEC/2017.

Conflicts of Interest: The authors declare no conflict of interest.

References

1. Menke, S.M.; Ran, N.A.; Bazan, G.C.; Friend, R.H. Understanding energy loss in organic solar cells: Toward a new efficiency regime. *Joule* **2018**, *2*, 25–35. [CrossRef]
2. Carella, A.; Borbone, F.; Centore, R. Research progress on photosensitizers for DSSC. *Front. Chem.* **2018**, *6*, 481. [CrossRef] [PubMed]
3. Wu, J.; Hao, S.; Lan, Z.; Lin, J.; Huang, M.; Huang, Y.; Fang, L.; Yin, S.; Sato, T. A thermoplastic gel electrolyte for stable quasi-solid-state dye-sensitized solar cells. *Adv. Funct. Mater.* **2007**, *17*, 2645–2652. [CrossRef]
4. Green, M.A.; Ho-Baillie, A. Perovskite solar cells: The birth of a new era in photovoltaics. *ACS Energy Lett.* **2017**, *2*, 822–830. [CrossRef]
5. Tumbul, A.; Aslan, F.; Göktaş, A.; Mutlu, I. All solution processed superstrate type Cu_2ZnSnS_4 (CZTS) thin film solar cell: Effect of absorber layer thickness. *J. Alloy. Compd.* **2019**, *781*, 280–288. [CrossRef]
6. Zhang, W.; Jin, W.; Fukushima, T.; Saeki, A.; Seki, S.; Aida, T. Supramolecular linear heterojunction composed of graphite-like semiconducting nanotubular segments. *Science* **2011**, *334*, 340–343. [CrossRef] [PubMed]
7. Tahir, M.; Khan, D.N.; Gul, S.; Wahab, F.; Said, S.M. Photovoltaic effect on the microelectronic properties of perylene/p-Si heterojunction devices. *J. Mater. Sci. Mater. Electron.* **2019**, *30*, 19463–19470. [CrossRef]
8. Aslan, F.; Arslan, F.; Tumbul, A.; Goktas, A. Synthesis and characterization of solution processed p-SnS and n-SnS_2 thin films: Effect of starting chemicals. *Opt. Mater.* **2022**, *127*, 112270. [CrossRef]
9. Houili, H.; Tutiš, E.; Batistić, I.; Zuppiroli, L. Investigation of the charge transport through disordered organic molecular heterojunctions. *J. Appl. Phys.* **2006**, *100*, 033702. [CrossRef]
10. Zeb, M.; Tahir, M.; Muhammad, F.; Mohd Said, S.; Mohd Sabri, M.F.; Sarker, M.R.; Hamid Md Ali, S.; Wahab, F. Amplified spontaneous emission and optical gain in organic single crystal quinquethiophene. *Crystals* **2019**, *9*, 609. [CrossRef]
11. Mishra, A.; Fischer, M.K.; Bäuerle, P. Metal-free organic dyes for dye-sensitized solar cells: From structure: Property relationships to design rules. *Angew. Chem. Int. Ed.* **2009**, *48*, 2474–2499. [CrossRef] [PubMed]
12. Aghazada, S.; Nazeeruddin, M.K. Ruthenium complexes as sensitizers in dye-sensitized solar cells. *Inorganics* **2018**, *6*, 52. [CrossRef]
13. Deng, K.; Cole, J.M.; Rawle, J.L.; Nicklin, C.; Chen, H.; Yanguas-Gil, A.; Elam, J.W.; Stenning, G.B. Dye nanoaggregate structures in MK-2, N3, and N749 dye center dot center dot center dot TiO_2 interfaces that represent dye-sensitized solar cell working electrodes. *Acs Appl. Energy Mater.* **2020**, *3*, 900–914. [CrossRef]
14. Lim, J.; Lee, M.; Balasingam, S.K.; Kim, J.; Kim, D.; Jun, Y. Fabrication of panchromatic dye-sensitized solar cells using pre-dye coated TiO_2 nanoparticles by a simple dip coating technique. *RSC Adv.* **2013**, *3*, 4801–4805. [CrossRef]
15. Alekseev, P.; Sharov, V.; Borodin, B.; Dunaevskiy, M.; Reznik, R.; Cirlin, G. Effect of the lattice mismatch on the efficiency of the GaAs nanowire/Si substrate solar cell. *J. Phys. Conf. Ser.* **2015**, *2015*, 012004. [CrossRef]

16. Hagfeldt, A.; Boschloo, G.; Sun, L.; Kloo, L.; Pettersson, H. Dye-sensitized solar cells. *Chem. Rev.* **2010**, *110*, 6595–6663. [CrossRef]
17. Lee, K.; Park, S.W.; Ko, M.J.; Kim, K.; Park, N.-G. Selective positioning of organic dyes in a mesoporous inorganic oxide film. *Nat. Mater.* **2009**, *8*, 665–671. [CrossRef]
18. Musyaro′ah; Huda, I.; Indayani, W.; Gunawan, B.; Yudhoyono, G.; Endarko. Fabrication and characterization dye sensitized solar cell (DSSC) based on TiO2/SnO2 composite. *AIP Conf. Proc.* **2017**, *1788*, 030062.
19. Chang, S.; Wong, K.Y.; Xiao, X.; Chen, T. Effective improvement of the photovoltaic performance of black dye sensitized quasi-solid-state solar cells. *RSC Adv.* **2014**, *4*, 31759–31763. [CrossRef]
20. Han, L.; Islam, A.; Chen, H.; Malapaka, C.; Chiranjeevi, B.; Zhang, S.; Yang, X.; Yanagida, M. High-efficiency dye-sensitized solar cell with a novel co-adsorbent. *Energy Environ. Sci.* **2012**, *5*, 6057–6060. [CrossRef]
21. Nazeeruddin, M.K.; Pechy, P.; Renouard, T.; Zakeeruddin, S.M.; Humphry-Baker, R.; Comte, P.; Liska, P.; Cevey, L.; Costa, E.; Shklover, V. Engineering of efficient panchromatic sensitizers for nanocrystalline TiO_2-based solar cells. *J. Am. Chem. Soc.* **2001**, *123*, 1613–1624. [CrossRef]
22. Uddin, S.I.; Tahir, M.; Aziz, F.; Sarker, M.R.; Muhammad, F.; Nawaz Khan, D.; Hamid Md Ali, S. Thickness optimization and photovoltaic properties of bulk heterojunction solar cells based on PFB–PCBM layer. *Energies* **2020**, *13*, 5915. [CrossRef]
23. Goktas, A.; Tumbul, A.; Aba, Z.; Kilic, A.; Aslan, F. Enhancing crystalline/optical quality, and photoluminescence properties of the Na and Sn substituted ZnS thin films for optoelectronic and solar cell applications; a comparative study. *Opt. Mater.* **2020**, *107*, 110073. [CrossRef]
24. Mikailzade, F.; Önal, F.; Maksutoglu, M.; Zarbali, M.; Göktaş, A. Structure and magnetization of polycrystalline $La_{0.66}Ca_{0.33}MnO_3$ and $La_{0.66}Ba_{0.33}MnO_3$ films prepared using sol-gel technique. *J. Supercond. Nov. Magn.* **2018**, *31*, 4141–4145. [CrossRef]
25. Abdullah, K.A.; Bakour, B. Influence of depletion region width on performance of solar cell under sunlight concentration. *Energy Procedia* **2011**, *6*, 36–45. [CrossRef]
26. Ahmed, H.; Doran, J.; McCormack, S. Increased short-circuit current density and external quantum efficiency of silicon and dye sensitised solar cells through plasmonic luminescent down-shifting layers. *Sol. Energy* **2016**, *126*, 146–155. [CrossRef]
27. Marques Lameirinhas, R.A.; Torres, J.P.N.; de Melo Cunha, J.P. A Photovoltaic Technology Review: History, Fundamentals and Applications. *Energies* **2022**, *15*, 1823. [CrossRef]
28. Suresh, B.V. *Solid State Devices and Technology*; Pearson Education: Chennai, India, 2010.
29. Koyyada, G.; Kumar Chitumalla, R.; Thogiti, S.; Kim, J.H.; Jang, J.; Chandrasekharam, M.; Jung, J.H. A new series of EDOT based co-sensitizers for enhanced efficiency of cocktail DSSC: A comparative study of two different anchoring groups. *Molecules* **2019**, *24*, 3554. [CrossRef]
30. Nazeeruddin, M.K.; Pechy, P.; Grätzel, M. Efficient panchromatic sensitization of nanocrystallineTiO_2 films by a black dye based on atrithiocyanato–ruthenium complex. *Chem. Commun.* **1997**, *18*, 1705–1706. [CrossRef]
31. Muhammad, F.; Tahir, M.; Zeb, M.; Kalasad, M.N.; Mohd Said, S.; Sarker, M.R.; Sabri, M.F.M.; Ali, S.H.M. Synergistic enhancement in the microelectronic properties of poly-(dioctylfluorene) based Schottky devices by CdSe quantum dots. *Sci. Rep.* **2020**, *10*, 1–13. [CrossRef]
32. Younas, M.; Harrabi, K. Performance enhancement of dye-sensitized solar cells via co-sensitization of ruthenium (II) based N749 dye and organic sensitizer RK1. *Sol. Energy* **2020**, *203*, 260–266. [CrossRef]
33. Tahir, M.; Ilyas, M.; Aziz, F.; Sarker, M.R.; Zeb, M.; Ibrahim, M.A.; Mohamed, R. Fabrication and microelectronic properties of hybrid organic–inorganic (poly (9, 9, dioctylfluorene)/p-Si) heterojunction for electronic applications. *Appl. Sci.* **2020**, *10*, 7974. [CrossRef]
34. Tahir, M.; Sayyad, M.H.; Wahab, F.; Khan, D.N. The electrical characterization of Ag/N-BuHHPDI/p-Si heterojunction by current–voltage characteristics. *Mod. Phys. Lett. B* **2013**, *27*, 1350080. [CrossRef]
35. Ali, S.; Tahir, M.; Mehboob, N.; Wahab, F.; Langford, S.J.; Mohd Said, S.; Sarker, M.R.; Julai, S.; Hamid Md Ali, S. Amino anthraquinone: Synthesis, characterization, and its application as an active material in environmental sensors. *Materials* **2020**, *13*, 960. [CrossRef] [PubMed]
36. Yakuphanoglu, F. Photovoltaic properties of hybrid organic/inorganic semiconductor photodiode. *Synth. Met.* **2007**, *157*, 859–862. [CrossRef]
37. Muhammad, F.; Tahir, M.; Zeb, M.; Uddin, S.I.; Ahmed, S. Enhancement in the microelectronic properties of a PFB–CdSe quantum dots nanocomposite based schottky barrier diode. *J. Electron. Mater.* **2019**, *48*, 5169–5175. [CrossRef]
38. Aydın, M.; Türüt, A. The electrical characteristics of Sn/methyl-red/p-type Si/Al contacts. *Microelectron. Eng.* **2007**, *84*, 2875–2882. [CrossRef]
39. Islam, Z.U.; Tahir, M.; Syed, W.A.; Aziz, F.; Wahab, F.; Said, S.M.; Sarker, M.R.; Md Ali, S.H.; Sabri, M.F.M. Fabrication and photovoltaic properties of organic solar cell based on zinc phthalocyanine. *Energies* **2020**, *13*, 962. [CrossRef]
40. Sharma, K.; Sharma, V.; Sharma, S. Dye-sensitized solar cells: Fundamentals and current status. *Nanoscale Res. Lett.* **2018**, *13*, 1–46. [CrossRef]
41. Chen, Z.; Chen, X.; Jia, Z.; Zhou, G.; Xu, J.; Wu, Y.; Xia, X.; Li, X.; Zhang, X.; Deng, C. Triplet exciton formation for non-radiative voltage loss in high-efficiency nonfullerene organic solar cells. *Joule* **2021**, *5*, 1832–1844. [CrossRef]

42. Pirashanthan, A.; Velauthapillai, D.; Robertson, N.; Ravirajan, P. Lithium doped poly (3-hexylthiophene) for efficient hole transporter and sensitizer in metal free quaterthiophene dye treated hybrid solar cells. *Sci. Rep.* **2021**, *11*, 20157. [CrossRef] [PubMed]
43. Lestini, E.; Andrei, C.; Zerulla, D. Linear self-assembly and grafting of gold nanorods into arrayed micrometer-long nanowires on a silicon wafer via a combined top-down/bottom-up approach. *PLoS ONE* **2018**, *13*, e0195859. [CrossRef] [PubMed]